Article

The Electrochemical Characterization of Nanostructured Bi₂Se₃ Thin Films in an Aqueous Na Electrolyte

Raimonds Meija [1],*, **Vitalijs Lazarenko** [1], **Anna Skrastina** [1], **Yelyzaveta Rublova** [1], **Jana Andzane** [1], **Vanda Voikiva** [1], **Arturs Viksna** [2] **and Donats Erts** [1,2]

[1] Institute of Chemical Physics, University of Latvia, LV-1586 Riga, Latvia; vitalijs.lazarenko@lu.lv (V.L.); anna.skrastina@lu.lv (A.S.); yelyzaveta.rublova@lu.lv (Y.R.); jana.andzane@lu.lv (J.A.); vanda.voikiva@lu.lv (V.V.); donats.erts@lu.lv (D.E.)
[2] Faculty of Chemistry, University of Latvia, LV-1586 Riga, Latvia; arturs.viksna@lu.lv
* Correspondence: raimonds.meija@lu.lv

Abstract: Due to their layered structure and high theoretical capacity, bismuth chalcogenides have been proposed as anodes in organic electrolyte Li- and Na-ion batteries. On the other hand, their electrochemical properties in aqueous systems have not been reported. Here, the electrochemical performance of Bi₂Se₃ thin films in 1 M NaNO₃ aqueous electrolyte is presented. This aqueous Bi₂Se₃ system was found to have up to two orders of magnitude increased diffusion coefficients, compared to other anode materials in Na electrolyte-based systems, as well as limited anode electrode degradation over 5 CVs and significant changes in the anode after 30 CVs.

1. Introduction

Effective storage of electrical energy is one of the greatest challenges in the world today [1]. With the growing usage of electrical vehicles, portable devices, and solar and wind energy power plants, which will require energy storage and redistribution units to manage short-run fluctuations in supply and demand, battery production is currently one of the major challenges. While lithium-ion batteries have shown the best performance on the production level and dominated the field of electrical energy storage since the 1990s [2], at the moment, they face issues such as geographically localized mining sites, as well as expensive and flammable electrolytes. Limited lithium resources and high demand may lead to limited availability and high costs of lithium-ion batteries in the future. To prevent this, research is currently underway in several directions.

One direction is to increase the energy and power density of battery electrode materials to reduce the number of individual cells needed, thus reducing the overall costs. It is possible to increase the energy and specific power of batteries by improving the anodes. Among the commercially used anodes, because of the reliable cycling performance, graphite has been the most popular one for 30 years. The main disadvantage of the graphite anode is its limited capacity and charging speed [3], and given the active development of chemical current sources and the expansion of their applications, the search for alternative anodes is an urgent task. Another direction that can significantly reduce the cost of batteries without losing their performance is the development of sodium-ion batteries. The abundance of Na (earth crust contains approx. 2.8% Na but contains only 20 ppm Li) and its affordability makes sodium-ion batteries a prospective alternative for the state-of-the-art LIBs that are used today. An additional advantage of sodium-ion batteries compared with lithium-ion batteries is, for example, the safety of their discharge to zero, which makes them easier to transport and store [4]. Therefore, research in the development of sodium-ion batteries is increasing exponentially every year.

Another crucial question in battery development is the choice of solvent for the electrolytes because solvents play key roles in ion transfer, as well as in determining the nature of discharge products and rechargeability. A suitable solvent should have a high dielectric constant and low viscosity; in addition, it should be inert to all cell components, be safe, non-toxic, and inexpensive [5]. Thus, aqueous electrolytes could be an attractive alternative for widely used organic solvents, as they are nonflammable, cheap, have a very high ionic conductivity, and therefore could operate at very high power [6]. Thereby, aqueous sodium-ion batteries (ASIBs) have attracted increased interest as next-generation batteries [7,8], especially for stationary energy storage plants [8], where the superior energy density of lithium-ion batteries is not significant, as they are not space-limited like electric vehicles and portable electronic devices.

The challenge with aqueous sodium-ion batteries is that most materials are not suitable as electrodes due to their insufficient electronic conductivity and electrochemical stability [9]. Overall, the materials that can be used as battery anodes can be divided into the following categories: materials based on intercalation, such as nanofibers and TiO_2, metals based on alloying mechanisms such as Sb or Bi, and metal (such as Sb and Bi) chalcogenides based on the two-step reaction mechanism, including conversion and alloying reactions [10].

In combination with liquid organic electrolytes, bismuth chalcogenide anodes Bi_2X_3 (X = Te, Se, S) have shown high theoretical volumetric (up to 4500 mAh/cm^3 for lithium-ion batteries) [11] and gravimetric capacities (~ 400–650 mAh/g for both lithium-ion and sodium-ion batteries) [12]. This was possible due to the unique structure of bismuth chalcogenides. For example, bismuth selenide in its crystal structure is a five-layer layer with a thickness of ~1 nm. Each layer of bismuth selenide consists of five-atomic covalently bonded Se^1–Bi–Se^2–Bi–Se^1 planes, these layers are connected through a weak Van der Waals interaction. Due to the layered structure of bismuth selenide and the large interlayer distance (d (015) = 3.04 Å), cations can intercalate into Van der Waals gaps [11,13]. Among the bismuth chalcogenides, Bi_2Se_3 displays a high electrical conductivity (two orders of magnitude higher than Bi_2S_3 [14]), which allows for a better rate performance and has a high density, enabling a possibility to produce devices with high theoretical volumetric capacities up to 3667 mAh·cm^{-3} [15], which is almost an order of magnitude higher than the commercial graphite for non-aqueous lithium-ion batteries (570 mAh·cm^{-3}) [16].

Bi_2Se_3 and its composites (e.g., with carbon allotropes) have shown promise as anode electrodes in non-aqueous electrolyte Na-ion battery cells [15]. However, to the best of our knowledge, an electrochemical investigation of Bi_2Se_3 as an anode electrode in aqueous electrolyte Na-ion cells has not been performed. In our study, an electrochemical investigation of physical vapor deposition (PVD) grown nanostructured Bi_2Se_3 thin films in aqueous electrolyte (1 M $NaNO_3$) was performed for the first time.

2. Experimental

2.1. Synthesis and Characterization of Bi_2Se_3 Thin Films

Synthesis was carried out in a controllable vacuum furnace on microscope glass slides (75 × 25 mm), using a principal physical vapor deposition method, developed in the laboratory [17]. A programmable quartz tube furnace (GLX-1100X, MTI Corp) was used. For the synthesis, 15 mg raw Bi_2Se_3 (Sigma-Aldrich, Burlington, MA, USA, 99.999%) was used, which was weighted in ceramic boats using analytical scales (KERN "ABP 200-5DM", ±0.01 mg). Quartz pipe (l = 60 cm, d = 4.5 cm) with adjustable valves on both sides was inserted inside the furnace. Raw Bi_2Se_3 (585 °C) and glass slides (330–380 °C) were placed at certain temperature regions inside this pipe. The quartz pipe was connected to the rotatory pump and nitrogen gas cylinder (Linde, Berlin, Germany, 99.999%). Before synthesis, the pipe was purged with nitrogen gas and vacuumed. After the vacuuming process, the quartz pipe was gradually heated up to 585 °C for 45 min and held at this temperature for 15 min at pressure 2–3 Torr. The physical vapor deposition process was stopped by reinjecting nitrogen gas into the pipe when it had cooled down to 470 °C.

The morphology and stoichiometry investigations of the synthesized Bi_2Se_3 thin films were performed using a Hitachi FE-SEM S-4800 scanning electron microscope (SEM), equipped with a Broker XFLASH 5010 energy-dispersive X-ray spectroscopy (EDX) sensor and an Asylum Research MFP-3D atomic force microscope. The samples with the appropriate structures were selected for electrochemical measurements.

2.2. Electrochemical Measurements

Electrochemical measurements were performed using a 3-electrode cell (Figure 1) and PalmSens4 potentiostat at room temperature. The setup was chosen to ensure an equal distance between the electrodes and the constancy of the working surface. The reference electrode (RE) was Ag/AgCl (3 M KCl), the counter electrode (CE) was Pt wire (ItalSens, PalmSens), and the working electrode (WE) was as-synthesized Bi_2Se_3 thin film (working area 0.19 cm^2). As an electrolyte, 1 M $NaNO_3$ (ThermoFisher, analytical grade 99%) was used. $NaNO_3$ was used instead of sulfur-based electrolytes because of the surface activity of the anions in sulfides and sulfites, as well as the possibility for the sulfates to exist in the form of several crystalline hydrates ($Bi_2(SO_4)_3 \cdot 3H_2O$; $Bi_2(SO_4)_3 \cdot 3.5H_2O$; $Bi_2(SO_4)_3 \cdot 7H_2O$). On the other hand, the structure of bismuth nitrate crystalline hydrate is well studied and is $Bi[(H_2O)_3(NO_3)_3] \cdot 2H_2O$ [18].
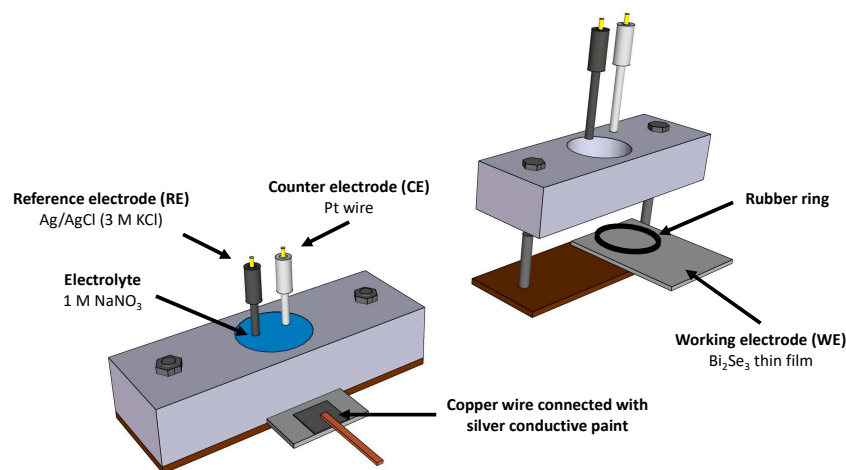
Figure 1. Schematics of the laboratory-made 3-electrode electrochemical cell.

To ensure a stable electrical contact during the electrochemical measurements, the part of the working electrode that was not in a contact with the electrode was covered with silver conductive paint (Electrolube) to which a copper wire was attached. Cycling voltammetry (CV) curves were measured in the potential range (-1.0 V $\div$ 1.3 V) at various scan rates (0.1 mVs^{-1} $\div$ 1.0 mVs^{-1}). The galvanostatic charge–discharge measurements were carried out with a current density of 90 mA/g.

EIS measurements were carried out in the frequency range 0.01–10,000 Hz, using open circuit potential. Spectra were acquired for a fresh sample and after the 1st, 5th, 10th, 20th, and 30th CV cycle. Spectra were analyzed using the Levenberg–Marquardt algorithm, the corresponding equivalent circuits were found, and the values of the respective circuit elements were determined.

After CV measurements, the working electrode (Bi_2Se_3 thin film) was washed with deionized water (4–5 times), dried at room temperature (25 °C), and investigated using SEM/EDX to analyze the structural and chemical changes in the electrode after the electrochemical measurements.

3. Results

3.1. Morphology of the Synthesized Structures

A synthesis method that promotes the growth of nanoplates with different angles against the substrate was selected to increase the surface area of the thin film Bi_2Se_3

electrode [17]. The thickness of the films was 500 nm, and the size of the nanoplates varied between 0.5 and 3 μm (Figure 2a). The EDX spectrum showed Si, Se, Bi, O, and C peaks. Si, O, and C peaks were background signals from the microscope and the substrate (Figure 2c). EDX quantitative analysis showed that synthesized samples were stochiometric, with an atomic ratio of 2:3 for Bi and Se, respectively (Table 1).
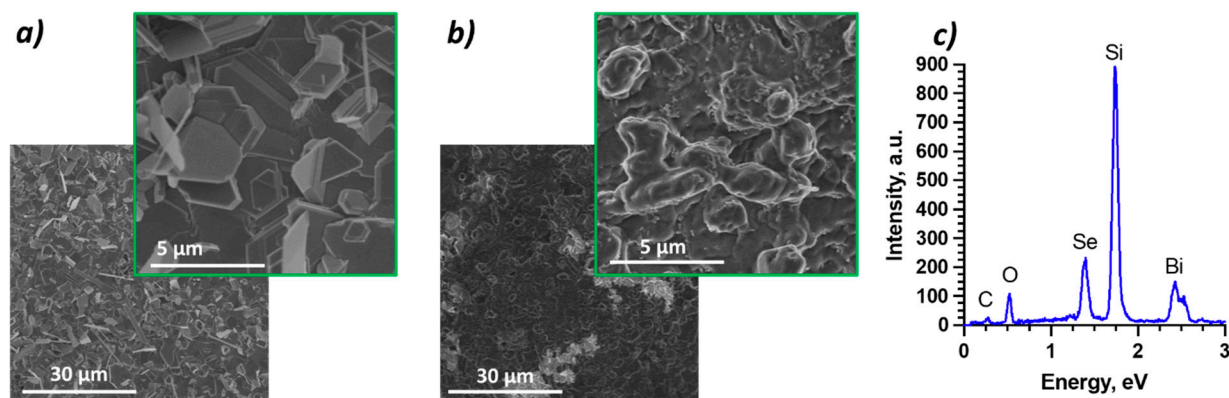
Figure 2. (**a**) SEM image of a fresh Bi_2Se_3 thin film; (**b**) SEM image of a fresh Bi_2Se_3 thin film after 5 CV cycles at scan rate 1.0 mVs^{-1}; (**c**) EDX spectra of a fresh sample.

Table 1. Quantitative EDX analysis before cycling and after 5 CV cycles at 0.25 mV·s^{-1} and after 30 CV cycles at 1 mV·s^{-1}. σ—standard deviation.

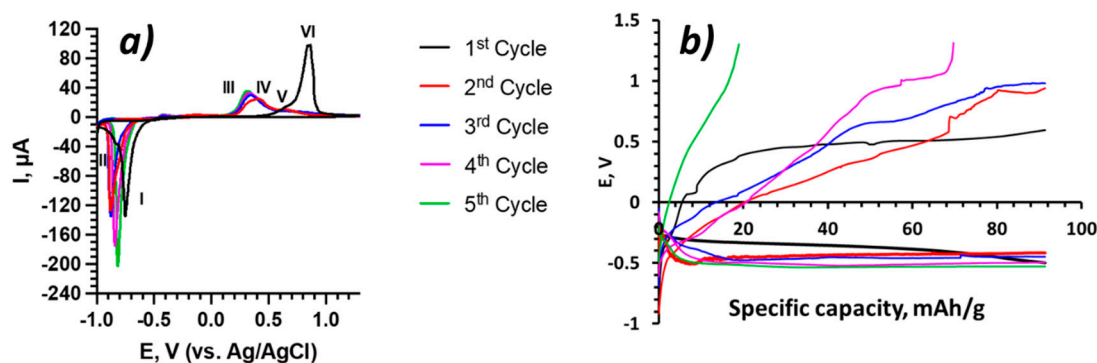|	Before Cycling			After 5 Cycles			After 30 Cycles		
Element	mass %	atomic %	3σ, mass %	mass %	atomic %	3σ, mass %	mass %	atomic %	3σ, mass %
Bismuth	58.53	27.03	5.29	45.71	10.19	3.44	29.51	4.31	2.24
Selenium	33.61	41.08	2.99	15.91	9.39	1.74	11.27	4.36	1.26
Oxygen	0.72	4.37	0.58	10.23	29.81	2.57	20.66	39.44	5.29
Nitrogen	0.70	4.84	0.67	1.73	5.76	0.61	5.84	12.74	1.89
Carbon	0.39	3.09	0.39	0.09	0.37	0.12	0.00	0.00	0.00
Silicon	2.73	9.37	0.41	10.00	16.60	0.96	2.51	2.73	0.31
Sodium	0.63	2.65	0.21	9.02	18.29	1.27	22.42	29.78	3.00
Magnesium	0.79	3.14	0.21	1.00	1.91	0.19	0.55	0.69	0.16
Potassium	0.01	0.02	0.08	2.25	2.68	0.23	3.10	2.42	0.30
Calcium	1.82	4.38	0.25	2.20	2.56	0.22	0.36	0.28	0.12
Chlorine	0.00	0.00	0.00	1.85	2.43	0.21	3.78	3.26	0.36

3.2. Electrochemical Measurements

Cyclic voltammetry curves in potential range (−1.0 V ÷ 1.3 V) at a scan rate of 0.25 mV s^{-1} showed two cathodic (I, II) and four anodic (III, IV, V, VI) peaks (Figure 3a). Peaks I and III represent reversible intercalation and deintercalation processes of Na$^+$ ions (Equation (1)), which occur in the interlayer space of Bi_2Se_3 thin films [19]. Peaks II and IV, which overlapped with peaks I and III, represent substitution reactions between Bi_2Se_3 and a water-soluble Na_2Se (Equation (2)) [15].

$$Bi_2Se_3 + xNa^+ + xe^- \leftrightarrow Na^+{}_x[Bi_2Se_3]^{x-} \qquad (1)$$

$$Bi_2Se_3 + 6Na^+ + 6e^- \leftrightarrow 3Na_2Se + 2Bi \qquad (2)$$

Anodic peak V represents the reduction of NO_3^- to NO_2^-, but in the presence of dissolved oxygen in the electrolyte, NO_2^- oxidizes back to NO_3^- (Equation (3)) [20]. Peak VI (0.86 V), which appeared only during the first cycle, indicates the development of a solid electrolyte interphase (SEI) layer, which probably consisted of Na_2O, Na_2O_2, and Na_2CO_3 (Equations (4)–(6)) [21] (Figure 3a).

$$NO_3^- + 2H^+ + 2e^- \leftrightarrow NO_2^- + H_2O \qquad (3)$$

$$4Na^+ + O_2 + 4e^- \rightarrow 2Na_2O \tag{4}$$

$$2Na^+ + O_2 + 2e^- \rightarrow Na_2O_2 \tag{5}$$

$$4Na^+ + 3CO_2 + 4e^- \rightarrow 2Na_2CO_3 \tag{6}$$
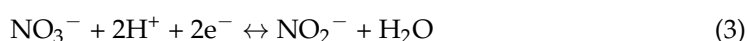
Figure 3. (**a**) Bi_2Se_3 thin films CVs at scan rate 0.25 mVs^{-1} and (**b**) charge–discharge curves at 90 mA/g in $-1.0 \div 1.3$ V vs. Ag/AgCl potential range.

Additionally, there was a tendency for the heights of peaks I and III, which correspond to the Na$^+$ intercalation–deintercalation processes, to increase gradually in subsequent cycles (Figure 3a), which may indicate a surface treatment of Bi_2Se_3, involving the development of an SEI layer on the surface of the anode. The heights of peaks II and IV, which represent conversion reactions, slowly decreased (Equation (2)), which indicates possible changes in Bi_2Se_3 and Na_2Se_3 amounts in the cell. During the first two cycles (first and second cycle), a significant shift of the intercalation peak (I) toward the negative potential side was observed. The shifts can indicate possible cycling-induced structural changes in Bi_2Se_3 thin films. In the following cycles, the process stabilized and the intensities of subsequent peaks began to coincide, which may hint at the end of pretreatment of the electrode.

Na$^+$ intercalation–deintercalation processes, which are represented by peaks I and III, were reversible but with different peak heights. That indicated two different mechanisms for these processes—intercalation is dominated by charge transfer, but deintercalation is dominated by thin-film mechanisms [22]. Further, intercalation is affected by the crystal lattice of the electrode, while deintercalation depends heavily on the interaction between the intercalated ions and is generally faster [22].

A comparison of Bi_2Se_3 thin film SEM images before and after five cycles of CV is shown in Figure 2a,b. It can be seen that, after the cycling, Bi_2Se_3 thin films were covered with an amorphous layer, which may indicate an SEI layer consisting of Na_2O, Na_2O_2, and Na_2CO_3 [21,23,24]. These changes were also confirmed by the acquired CVs (Figure 3a). EDX analysis (Table 1) of the samples after cycling showed that only a small amount of Se dissolved (~10 percentage points), which indicates limited dissolubility of the Se in the electrode in 1 M NaNO$_3$ in the first five cycles.

To investigate how the structure of nanostructured Bi_2Se_3 thin films changed during extended cycling, 30 CVs were obtained at the scan rate of 1.0 mVs^{-1} (Figure 4).

Continuous cycling showed that the intercalation peak (I) gradually shifted toward the negative potential from -0.59 V (1st cycle) to -0.65 V (10th cycle) and maintained the peak height above -100 μA up to 13th cycle, at which point the intercalation peak began to rapidly shift (approx. by -0.2 V per cycle) toward the negative potential, and the intercalation peak height diminished rapidly, becoming -58 μA at 20th cycle and -31 μA at 30th cycle. For the deintercalation peak (III), similar tendencies were observed—the peak voltage was stable around 0.26 V until the 7th cycle, after which it dropped to 0.03 V, around which it stayed until the 30th cycle. The deintercalation peak (III) current was above 40 μA until the 26th cycle and decreased down to 36 μA at the 30th cycle. The significant intercalation (I) and deintercalation (III) peak shifts that occurred during cycling toward negative potential indicate significant changes in the anode, such as irreversible reactions,

structural degradation, and buildup of residue that may impede the charge–discharge processes, as observed in SEM images and EDX spectra after 30 cycles (Supplementary Figure S1, Table 1).
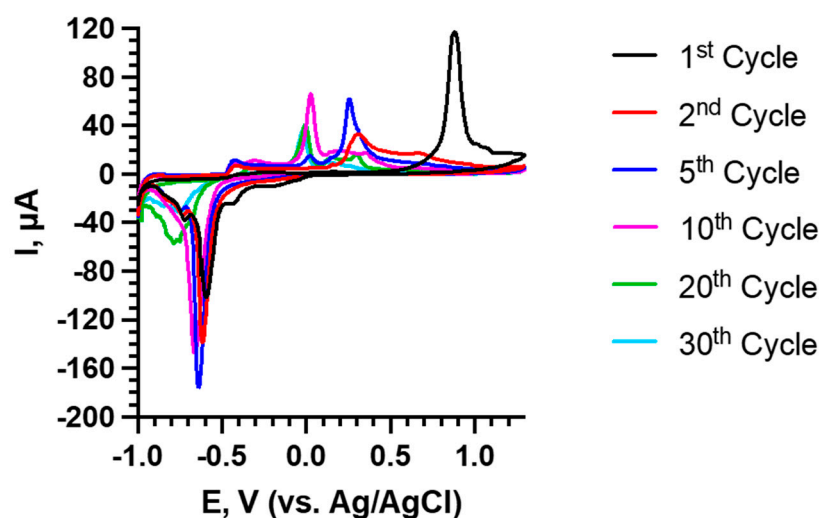
**Figure 4.** Bi_2Se_3 thin films CVs in $-1.0 \div 1.3$ V vs. Ag/AgCl potential range at scan rate 1.0 mVs^{-1}, 30 cycles.

The galvanostatic charge–discharge profiles (90 mA/g) of the first five cycles (Figure 3b) showed a wide charge plateau at -0.41 V for the first cycle, which corresponds to the sodium intercalation, and shifted to the negative potentials during subsequent cycles. The discharge profiles showed the formation of the SEI layer at 0.5 V at the first cycle and the galvanostatic capacity of 90 mAh/g in the second and third cycles.

It should be noted that the performance of the anode is affected by the solvation of Na^+ in a water–electrolyte solution. Solvated Na^+ ions, when they approach the electrode surface, first need to be at least partially desolvated, and only then can enter the interplanar space. If the intercalated ion is partially hydrated, the coordinated water molecules shield the positive charge of the cations, thus mitigating the repulsion force of the Na^+ ions. Thus, modification of the electrode material, to make it more hydrophilic, as well as pre-intercalation with water, may improve its performance [25].

EIS measurements were carried out both before the cycling and after a predetermined cycle number (1st, 5th, 10th, 20th, and 30th), which allowed the estimation of the electrochemical cycling-induced changes in Bi_2Se_3 thin films. Analysis of Nyquist plots (Figure 5a) revealed electrolyte resistance (R_{el}) at the Z' axis cross-section at large frequencies. The semicircle at the medium-frequency range represents charge transfer resistance (R_{ct}), and the linear part of the plot at the low-frequency range indicates the Warburg element, which represents the Na^+ diffusion in Bi_2Se_3 interplanar space. After the first cycle, and also after the following cycles, an additional small semicircle can be observed in the low-frequency range, which represents the resistance R_{SEI} of the SEI layer (Figure 5a). This assumption was supported by the CV data (Figure 4). The determined equivalent circuits (Figure 5b) showed constant phase elements both for Bi_2Se_3 thin films (CPE_{ct}) and SEI layer (CPE_{SEI}), indicating the increased roughness of the electrode (AFM measurements showed an increase in R_a from 73 nm to 116 nm for a 100 μm^2 large section of the electrode) and the unevenness of the SEI layer (Supplementary Figures S1 and S2).

The quantitative values of R_{el}, R_{ct}, R_{SEI}, CPE_{SEI}, CPE_{CT}, and W were determined using the Levenberg–Marquardt algorithm. The acquired results (Table 2) show that R_s was stable (40 ± 2 $\Omega \cdot cm^2$) during the cycling, which indicates a stable electrolyte during 30 cycles. The formation of the SEI layer on the electrode surface after the first cycling significantly changed the behavior of the Bi_2Se_3 thin film. The formed SEI layer is an ionic conductor, which is characterized by a significant increase in the values of the Warburg element (from

16 to 756 $\Omega \cdot s^{-1/2}$). In our study, the Warburg element revealed Na^+ diffusion in Bi_2Se_3 interplanar space. During 30 cycles, the value of the Warburg element fluctuated within $750 \div 900\ \Omega\ s^{-1/2}$, which indicates a stable diffusion of sodium ions during the experiment. In addition to its contribution to diffusion, the formation of the SEI layer also led to kinetic changes, which were characterized by a decrease in R_{ct} by a factor of 1.8 and an increase in CPE_{ct} by more than two orders of magnitude (from 4 to 553 $\Omega^{-1} \cdot s^{-n}$; Table 2). It is also worth noting that a gradual increase in R_{ct} was observed during cycling, which indicates the appearance of additional kinetic limitations. A decrease in CPE_{ct} indicates irreversible changes on the surface of a thin film (Supplementary Figure S1). Additionally, during cycling, a decrease in the parameters R_{SEI} (from 273 to 40 $\Omega \cdot cm^{-2}$) and CPE_{SEI} (from 365 to 71 $\Omega^{-1}\ s^{-n}$) was observed, which can be caused by the gradual dissolution of Na_2O, Na_2O_2, and Na_2CO_3 from the surface of the Bi_2Se_3 thin film.
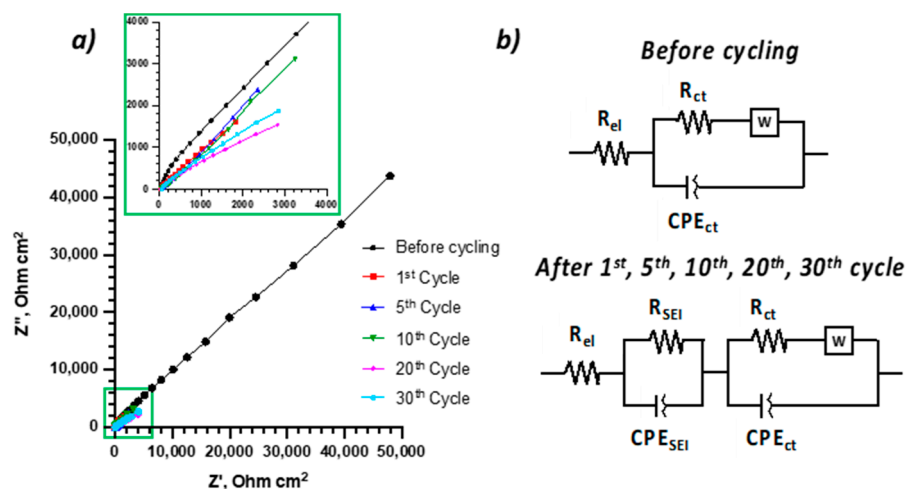
Figure 5. (**a**) Nyquist plots after predetermined CV cycle number; (**b**) determined equivalent circuits of the system.

Table 2. Impedance spectra equivalent circuit element values after different CV cycles.

	Fresh Sample	After the 1st Cycle	After the 5th Cycle	After the 10th Cycle	After the 20th Cycle	After the 30th Cycle
Rel, $\Omega \cdot cm^2$	36	41	41	39	43	41
R_{SEI}, $\Omega \cdot cm^2$	-	273	157	96	58	40
CPE_{SEI}, $\Omega^{-1}\ s^{-n}$	-	365	379	111	126	71
R_{ct}, $\Omega \cdot cm^2$	1596	900	1010	1155	1178	1221
CPE_{ct}, $\Omega^{-1}\ s^{-n}$	4	553	398	272	95	57
W, $\Omega \cdot s^{-1/2}$	16	756	809	785	759	896

To determine the dominant process in intercalation and deintercalation (Figure 6), CVs at different scan rates from 0.1 to 1.0 mVs^{-1} were acquired for the second and third cycles, which show a stable electrode performance. The second and third cycles were chosen because, during the first cycle, SEI layer growth on the electrode surface occurred; thus, the second and third cycles revealed a situation in which electrode pretreatment was finished, and the electrode was still relatively unaffected by the electrochemical cycling, making the kinetic measurements representative of the Bi_2Se_3 anode material.

From Equation (7), and using peaks I and III (Figure 6), it was determined that, during the second and third cycle, the dominant process for Na^+ intercalation and deintercalation was capacitive ($b > 0.85$) [26], and it included pseudo-capacitive, capacitive, and electrical double-layer capacitive processes (Figure 7).

$$I = av^b \tag{7}$$

where *I*—current for Na$^+$ intercalation–deintercalation (mA); *v*—scan rate (mV s^{-1}); *a*, *b*—fitting parameters for a linear graph.
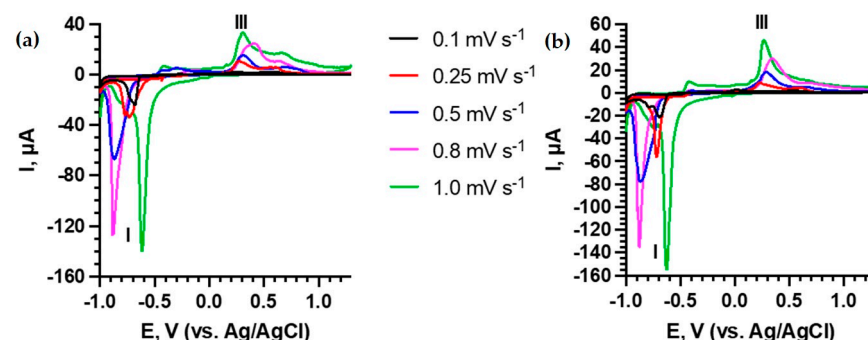
Figure 6. CVs for Bi$_2$Se$_3$ thin films with various scan rates (0.1—1.0 mV s^{-1}): (**a**) 2nd cycle; (**b**) 3rd cycle.
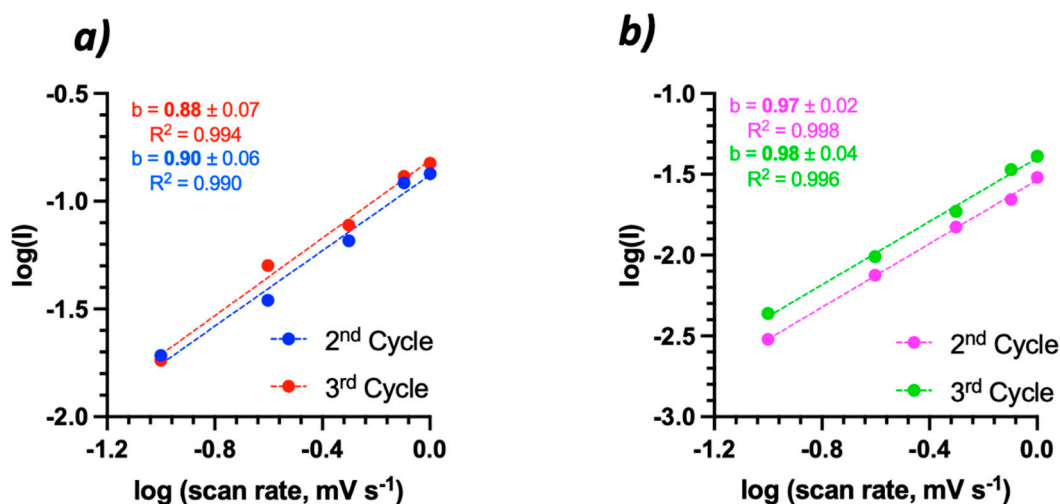
Figure 7. Log-scale plots of Bi$_2$Se$_3$ thin films in 1 M NaNO$_3$: (**a**) Na$^+$ intercalation; (**b**) Na$^+$ deintercalation.

A closer investigation on the capacitive contribution (Equation (8)) shows that at the scan rate 0.1 mV s^{-1}, the process was diffusion-controlled (second cycle—58.5%; third cycle—61.0%). On the other hand (Figure 8), at faster cycling speeds (0.25—1.0 mV s^{-1}), it is capacitive process dominated (>50%). The high capacitive contribution could indicate a rapid charge transfer process, as well as the diminishing of the Na$^+$ diffusion barrier during the intercalation–deintercalation.

$$i(V) = k_1 v + k_2 v^{1/2} \tag{8}$$

where *i*(*V*)—Na$^+$ current for Na$^+$ intercalation–deintercalation (mA); $k_1 v$—contribution of the capacitive process; $k_2 v^{1/2}$—contribution of the diffusive process.

Na$^+$ diffusion coefficients during intercalation–deintercalation were determined from the slopes of Figure 9, using Equation (9).

$$D = \left(\frac{slope}{0.446 nFAC}\right)^2 \left(\frac{RT}{nF}\right), \tag{9}$$

where *D*—diffusion coefficient (cm^2 s^{-1}); *slope*—the slope of the graph; *n*—number of electrons that participate in a reaction; *F*—Faraday constant (C mol^{-1}); *A*—surface area of the electrode (cm^2); *C*—electrolyte concentration (mol cm^{-3}); *R*—universal gas constant (J K^{-1} mol^{-1}); *T*—temperature (K).
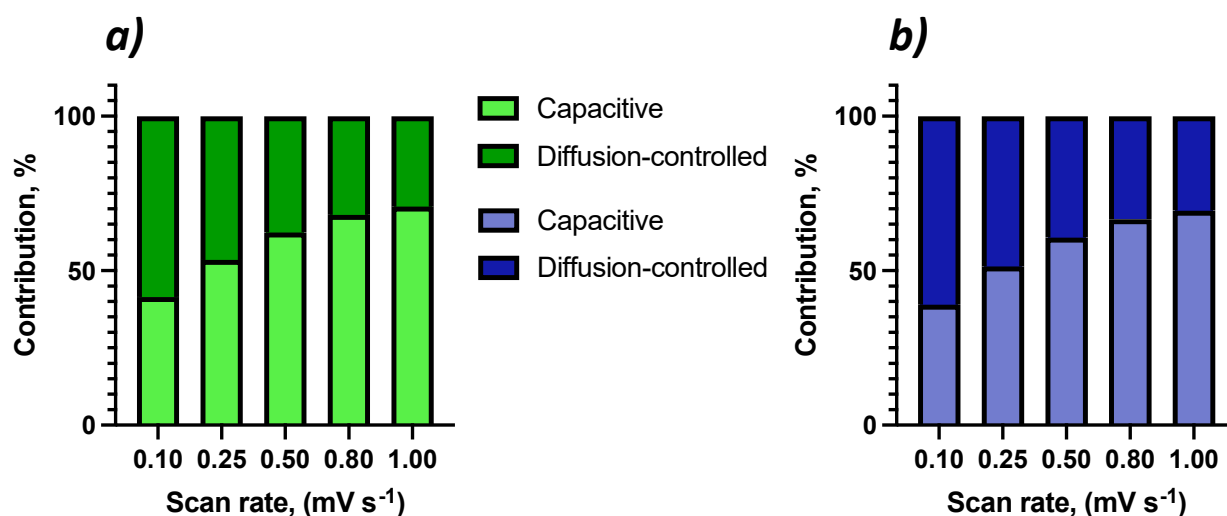
Figure 8. The contribution of capacitive and diffusion-controlled processes of Bi_2Se_3 thin-film in 1 M $NaNO_3$: (**a**) 2nd cycle; (**b**) 3rd cycle.
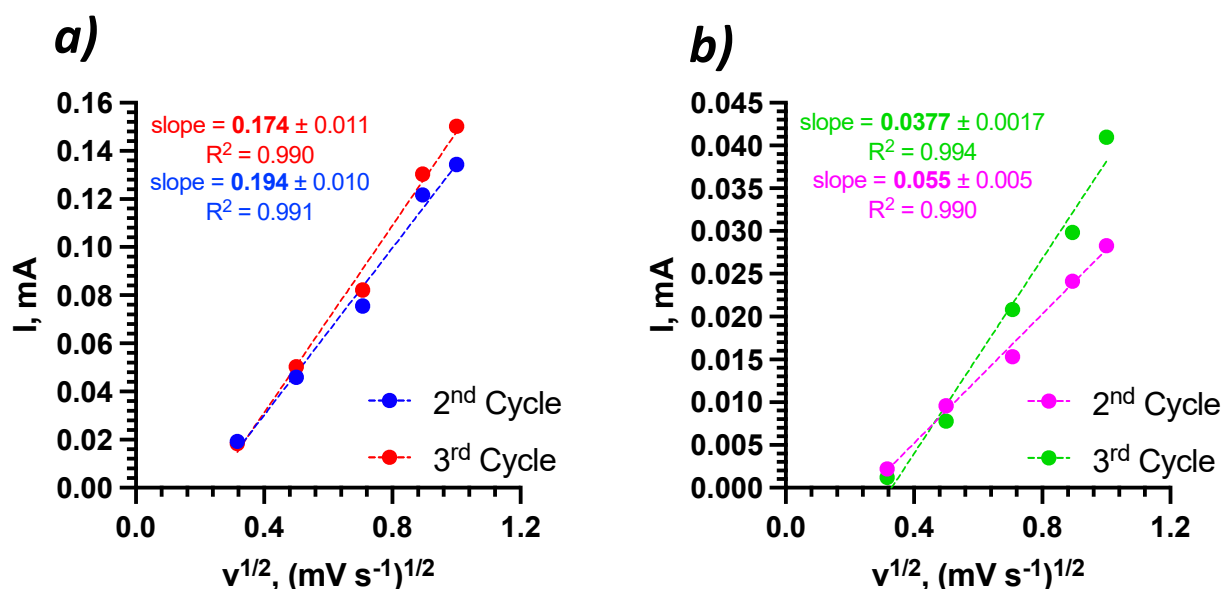
Figure 9. The dependence of $v^{1/2}$ vs. I of Bi_2Se_3 thin film in 1 M $NaNO_3$ in the 2nd and 3rd cycles with fitted slope values for (**a**) Na^+ intercalation and (**b**) Na^+ deintercalation.

The calculated Na^+ diffusion coefficient values (Table 3) show that the diffusion coefficients for intercalation were higher by ~1–2 orders of magnitude than those for deintercalation, indicating different reaction mechanisms, which were also confirmed by the acquired CVs (Figure 6). The comparison with diffusion coefficients for non-aqueous systems in which Bi_2Se_3 was used as an electrode shows that the diffusion coefficient for intercalation was two orders of magnitude higher than that in the aqueous system. The aqueous system's diffusion coefficient for deintercalation was also 2–3 magnitudes higher than that for pure Bi_2Se_3 electrodes in the non-aqueous electrolyte and was comparable with Bi_2Se_3/CC heterostructure non-aqueous electrolyte, which is expected, as the added carbon cloth can provide a preferable architecture for ion diffusion [27]. It must also be noted that the effect of thickness should be considered when comparing different anode materials. Very large (higher than 200 µm) electrode thickness has a negative impact on the diffusion coefficient, as ions cannot penetrate the material and agglomerate on the surface of the electrode, thus saturating it and also enhancing the degradation risk [28]. As shown in Table 3, compared electrodes had thicknesses that were an order of magnitude lower

than 200 μm; in these electrodes, the morphology of the electrodes affect the diffusion coefficient the most.

Table 3. Na^+ intercalation–deintercalation diffusion coefficient (cm^2 s^{-1}) comparison with other anodes–electrolytes.

Electrode	Thickness	Electrolyte	Intercalation	Deintercalation	Cycle	Reference
Bi_2Se_3 thin film	500 nm	1 M $NaNO_3$	1.1×10^{-11} 1.4×10^{-11}	5.1×10^{-13} 1.1×10^{-12}	2nd 3rd	This work
Bi_2Se_3/CC [a]	1–20 μm *	1 M $NaClO_4$ EC/PC (1:1)	2.2×10^{-13}—9.7×10^{-12}		1st	[27]
Bi_2Se_3 microspheres	1–20 μm *	1 M $NaClO_4$ EC/PC (1:1)	9.3×10^{-13}	5.7×10^{-15}	1st	[27]

[a] Bi_2Se_3 nanocrystalline array grown on flexible conductive carbon cloth. * Authors did not provide the thickness of the electrode; therefore, values estimated from the loading factor and the density of the materials in the electrode.

4. Conclusions

In this study, the electrochemical performance of nanostructured Bi_2Se_3 thin film as an anode in 1 M $NaNO_3$ aqueous electrolyte was investigated. CV and EIS investigations showed that an unstable SEI layer formed in the first cycle at the potential 0.86 V. CVs at 1 mV·s^{-1} and subsequent EIS measurements showed stable electrolyte performance (R_{el}) and a gradual increase in R_{ct}, which indicates the emergence of additional kinetic limitations, while R_{SEI} decreased significantly (>6 times). A long-term CV investigation consisting of 30 cycles with the scan rate of 1.0 mV·s^{-1} showed a gradual degradation in the Bi_2Se_3 thin film, consistent with the EIS measurements. It was also determined that at lower scan rates ($\leq$0.1 mV·s^{-1}), the intercalation–deintercalation was dominated by the capacitive process, while at higher scan rates ($\geq$0.25 mV·s^{-1}), it became dominantly diffusion controlled. In comparison with Bi_2Se_3-based anode materials in aqueous Na electrolytes, our Bi_2Se_3 thin film-based system revealed up to two orders of magnitude increased diffusion coefficients.

References

1. Olabi, A.G.; Onumaegbu, C.; Wilberforce, T.; Ramadan, M.; Abdelkareem, M.A.; Alami, A.H.A. Critical review of energy storage systems. *Energy* **2021**, *214*, 118987. [CrossRef]
2. Manthiram, A. Materials Challenges and Opportunities of Lithium Ion Batteries. *J. Phys. Chem. Lett.* **2011**, *2*, 176–184. [CrossRef]

3. Cai, W.; Yao, Y.-X.; Zhu, G.-L.; Yan, C.; Jiang, L.-L.; He, C.; Huang, J.-Q.; Zhang, Q. A review on energy chemistry of fast-charging anodes. *Chem. Soc. Rev.* **2020**, *49*, 3806–3833. [CrossRef] [PubMed]

4. Sawicki, M.; Shaw, L.L. Advances and challenges of sodium ion batteries as post lithium ion batteries. *RSC Adv.* **2015**, *5*, 53129–53154. [CrossRef]

5. Roth, E.P.; Orendorff, C.J. How electrolytes influence battery safety. *Electrochem. Soc. Interface* **2012**, *21*, 45–49. [CrossRef]

6. Cresce, A.; Xu, K. Aqueous lithium-ion batteries. *Carbon Energy* **2021**, *3*, 721–751. [CrossRef]

7. Liu, Z.; Huang, Y.; Huang, Y.; Yang, Q.; Li, X.; Huang, Z.; Zhi, C. Voltage issue of aqueous rechargeable metal-ion batteries. *Chem. Soc. Rev.* **2020**, *49*, 180–232. [CrossRef] [PubMed]

8. Kim, H.; Hong, J.; Park, K.Y.; Kim, H.; Kim, S.W.; Kang, K. Aqueous Rechargeable Li and Na Ion Batteries. *Chem. Rev.* **2014**, *114*, 11788–11827. [CrossRef] [PubMed]

9. Yin, X.; Sarkar, S.; Shi, S.; Huang, Q.; Zhao, H.; Yan, L.; Zhao, Y.; Zhang, J. Recent Progress in Advanced Organic Electrode Materials for Sodium-Ion Batteries: Synthesis, Mechanisms, Challenges and Perspectives. *Adv. Funct. Mater.* **2020**, *30*, 1908445. [CrossRef]

10. Zhang, W.; Zhang, F.; Ming, F.; Alshareef, H.N. Sodium-ion battery anodes: Status and future trends. *Energy Chem.* **2019**, *1*, 100012. [CrossRef]

11. Ni, J.; Bi, X.; Jiang, Y.; Li, L.; Lu, J. Bismuth chalcogenide compounds Bi2×3 (X=O, S, Se): Applications in electrochemical energy storage. *Nano Energy* **2017**, *34*, 356–366. [CrossRef]

12. Sun, J.; Li, M.; Oh, J.A.S.; Zeng, K.; Lu, L. Recent advances of bismuth based anode materials for sodium-ion batteries. *Mater. Technol.* **2018**, *33*, 563–573. [CrossRef]

13. Hu, Z.; Liu, Q.; Chou, S.-L.; Dou, S.-X. Advances and Challenges in Metal Sulfides/Selenides for Next-Generation Rechargeable Sodium-Ion Batteries. *Adv. Mater.* **2017**, *29*, 1700606. [CrossRef]

14. Liu, W.; Lukas, K.C.; McEnaney, K.; Lee, S.; Zhang, Q.; Opeil, C.P.; Chen, G.; Ren, Z. Studies on the Bi_2Te_3–Bi_2Se_3–Bi_2S_3 system for mid-temperature thermoelectric energy conversion. *Energy Environ. Sci.* **2013**, *6*, 552–560. [CrossRef]

15. Xie, L.; Yang, Z.; Sun, J.; Zhou, H.; Chi, X.; Chen, H.; Li, A.X.; Yao, Y.; Chen, S. Bi_2Se_3/C Nanocomposite as a New Sodium-Ion Battery Anode Material. *Nano-Micro Lett.* **2018**, *10*, 50. [CrossRef] [PubMed]

16. Chae, S.; Choi, S.H.; Kim, N.; Sung, J.; Cho, J. Integration of Graphite and Silicon Anodes for the Commercialization of High-Energy Lithium-Ion Batteries. *Angew. Chem. Int. Ed.* **2020**, *59*, 110–135. [CrossRef]

17. Andzane, J.; Buks, K.; Strakova, M.N.; Zubkins, M.; Bechelany, M.; Marnauza, M.; Baitimirova, M.; Erts, D. Structure and Doping Determined Thermoelectric Properties of Bi_2Se_3 Thin Films Deposited by Vapour-Solid Technique. *IEEE Trans. Nanotechnol.* **2019**, *18*, 948–954. [CrossRef]

18. Lazarini, F. Redetermination of the structure of bismuth(III) nitrate pentahydrate, $Bi(NO_3)_3 \cdot 5H_2O$. *Acta Crystallogr. Sect. C Cryst. Struct. Commun.* **1985**, *41*, 1144–1145. [CrossRef]

19. Xu, B.; Qi, S.; He, P.; Ma, J. Antimony- and Bismuth-Based Chalcogenides for Sodium-Ion Batteries. *Chem. An Asian J.* **2019**, *14*, 2925–2937. [CrossRef]

20. Xin, X.; Ito, K.; Dutta, A.; Kubo, Y. Dendrite-Free Epitaxial Growth of Lithium Metal during Charging in Li–O 2 Batteries. *Angew. Chem.* **2018**, *130*, 13390–13394. [CrossRef]

21. Lee, M.H.; Kim, S.J.; Chang, D.; Kim, J.; Moon, S.; Oh, K.; Park, K.Y.; Seong, W.M.; Park, H.; Kwon, G.; et al. Toward a low-cost high-voltage sodium aqueous rechargeable battery. *Mater. Today* **2019**, *29*, 26–36. [CrossRef]

22. Noel, M.; Rajendran, V. A comprehensive model for cyclic voltammetric study of intercalation/de-intercalation process incorporating charge transfer, ion transport and thin layer phenomena. *J. Power Sources* **2000**, *88*, 243–249. [CrossRef]

23. Kim, S.; Jung, Y.; Park, J.; Hong, M.; Byon, H.R. Sodium fluoride-rich solid electrolyte interphase for sodium–metal and sodium–oxygen batteries. *Bull. Korean Chem. Soc.* **2021**, *42*, 1519–1523. [CrossRef]

24. Jin, T.; Ji, X.; Wang, P.F.; Zhu, K.; Zhang, J.; Cao, L.; Chen, L.; Cui, C.; Deng, T.; Liu, S.; et al. High-Energy Aqueous Sodium-Ion Batteries. *Angew. Chem. Int. Ed.* **2021**, *60*, 11943–11948. [CrossRef] [PubMed]

25. Xiao, B. Intercalated water in aqueous batteries. *Carbon Energy* **2020**, *2*, 251–264. [CrossRef]

26. Mathis, T.S.; Kurra, N.; Wang, X.; Pinto, D.; Simon, P.; Gogotsi, Y. Energy Storage Data Reporting in Perspective—Guidelines for Interpreting the Performance of Electrochemical Energy Storage Systems. *Adv. Energy Mater.* **2019**, *9*, 1902007. [CrossRef]

27. Dai, S.; Wang, L.; Shen, Y.; Wang, M. Bismuth selenide nanocrystalline array electrodes for high-performance sodium-ion batteries. *Appl. Mater. Today* **2020**, *18*, 100455. [CrossRef]

28. Gao, H.; Wu, Q.; Hu, Y.; Zheng, J.P.; Amine, K.; Chen, Z. Revealing the Rate-Limiting Li-Ion Diffusion Pathway in Ultrathick Electrodes for Li-Ion Batteries. *J. Phys. Chem. Lett.* **2018**, *9*, 5100–5104. [CrossRef] [PubMed]